Research Article Vol. 15, No. 8 / 1 Aug 2025 / Optical Materials Express 1924
Optical Materials EXPRESS

Growth, spectroscopy, and laser operation of Yb:$LaLuO_3$

Sascha Kalusniak,[1] Christo Guguschev,[1] Ramazan Koc,[1] Roberts Blukis,[1] Christian Rhode,[1] Jan Čejka,[2] Andrea Dittmar,[1] Darrell G. Schlom,[1,3,4] and Christian Kränkel[1,*]

[1]Leibniz-Institut für Kristallzüchtung (IKZ), Max-Born-Str. 2, 12489 Berlin, Germany
[2]Department of Solid State Chemistry, University of Chemistry and Technology, Technická 5, 166 28 Prague 6 – Dejvice, Czech Republic
[3]Department of Materials Science and Engineering, 210 Bard Hall, Cornell University, Ithaca, NY 14853-1501, USA
[4]Kavli Institute at Cornell for Nanoscale Science, 430 Physical Sciences Building, Cornell University, Ithaca, NY 14853-1501, USA
*christian.kraenkel@ikz-berlin.de

Abstract: We present the growth, chemical and structural characterization, optical spectroscopy, and first laser experiments of Yb:$LaLuO_3$. A high-optical-quality boule was grown, and the *Pnma* lattice structure was confirmed. Structural analysis reveals an anti-site fraction of 4-5% where Lu^{3+} and Yb^{3+} ions partially occupy La^{3+} sites. Due to an inversion symmetry of the primary doping ion site, we observe significant magnetic dipole contributions to the transition cross-sections, while the absolute cross-section values remain within the range typical for Yb^{3+}-doped materials. Fluorescence studies reveal a double-exponential decay behavior, with lifetimes of 2.06 ms and 0.31 ms and an integrated average fluorescence lifetime of 1.46 ms. The material exhibits a broad gain bandwidth exceeding 60 nm for all polarizations. In laser experiments, we achieved slope efficiencies of up to 75%, with output wavelengths ranging from 1044 nm to 1123 nm. These results highlight the potential of Yb:$LaLuO_3$ as a promising gain material for generating femtosecond pulses in mode-locked oscillators and for tunable laser applications in the 1.1 µm wavelength range.

1. Introduction

The growth of bulk $LaLuO_3$ crystals was first demonstrated in 1998 [1]. Since then, this material has been investigated for various applications. Its unusually large pseudocubic lattice constant makes it a demanded substrate material for the growth of strain-engineered thin films [2], and its high dielectric constant k makes it suitable for high-k gate dielectrics [3].

The 4f-shell of La^{3+} is empty, while that of Lu^{3+} is completely filled. Therefore, $LaLuO_3$ exhibits a wide transparency range with no intrinsic absorption peaks. This feature also makes ion-doped $LaLuO_3$ attractive for optical applications. Due to its high density and the high atomic number of lutetium, Ce^{3+}-doped $LaLuO_3$ is desired for efficient scintillator materials [4]. Recently, Guo *et al.* reported on optical floating zone (OFZ) growth and unpolarized, temperature-dependent optical characterization of Yb^{3+}-doped $LaLuO_3$ [5], indicating this material's potential for 1-µm laser operation. Despite its promising properties, reports on the successful growth of bulk $LaLuO_3$ crystals have remained limited, which we attribute to its high melting temperature of 2120 °C [1], posing a significant challenge to synthesis.

Here, we report on the Czochralski growth of Yb:$LaLuO_3$ and present a detailed chemical and structural analysis of this material. For the first time, we present polarization-dependent spectroscopic properties of Yb:$LaLuO_3$. Moreover, to the best of our knowledge, we demonstrate

#565169 https://doi.org/10.1364/OME.565169
Journal © 2025 Received 16 Apr 2025; revised 23 May 2025; accepted 3 Jun 2025; published 16 Jul 2025

Optical Materials EXPRESS

the first laser using this material. Laser operation with slope efficiencies of up to 75% was obtained under 970 nm pumping. The observed laser wavelengths between 1044 nm and 1123 nm indicate a strong potential for widely tunable laser operation and ultrashort mode-locked pulses.

2. Properties of $LaLuO_3$ crystals

Unlike disordered mixed cubic sesquioxides such as $(Y,Sc)_2O_3$ [6], $LaLuO_3$ is an ordered crystal. According to the Goldschmidt rule [7], inter-lanthanide oxides of the form $LnLn'O_3$, with a sufficient size ratio between the two trivalent lanthanide ions Ln and Ln', crystallize in a perovskite structure ABO_3, where A denotes the larger cation site and B the smaller one. Various inter-lanthanide compositions including those with La^{3+}, Ce^{3+}, Pr^{3+} and Nd^{3+} on the Ln (= A) site and Ho^{3+}, Er^{3+}, Tm^{3+}, Yb^{3+} and Lu^{3+} on the Ln' (= B) site have been synthesized in the past [8,9] and studied with respect to their optical [1], dielectric [9], and magnetic properties [10].

Among all inter-lanthanide oxide crystals, $LaLuO_3$ is the only suitable host material for rare-earth-doped solid-state lasers due to the absence of optically active ions, that would interfere with the laser process. However, additional requirements for laser host materials include the availability of suitable doping ion sites. In fact, the situation appears favorable in $LaLuO_3$. According to the lanthanide contraction rule, lighter and thus larger rare-earth ions preferentially occupy the La^{3+}-site, while heavier and thus smaller rare-earth ions tend to occupy Lu^{3+}-sites. Nevertheless, the symmetry of the coordination environment of a doping ion site must be considered. In particular, inversion-symmetric site environments preserve the symmetry of the rare-earth ions' 4*f* orbitals and the corresponding transitions remain Laporte-forbidden, resulting in low transition cross-sections.

The ideal perovskite structure is cubic, but the exact structure modification of an inter-lanthanide oxide depends on the ionic radii ratio of Ln and Ln': Typically, inter-lanthanide oxides with a large ionic size difference [8] crystallize in the orthorhombically distorted perovskite structure – *Pnma* (Nr. 62) shown in Fig. 1. Therefore, this structure is expected for the combination of the largest lanthanide ion La^{3+} and the smallest Lu^{3+}, *i.e.* $LaLuO_3$. This distortion causes tilting of the octahedral coordination polyhedra around the Lu^{3+} ions, which reduces the coordination number of the larger La^{3+} ions from 12, observed in the ideal cubic perovskite structure, to 8, while the Lu^{3+}-site remains 6-fold coordinated.

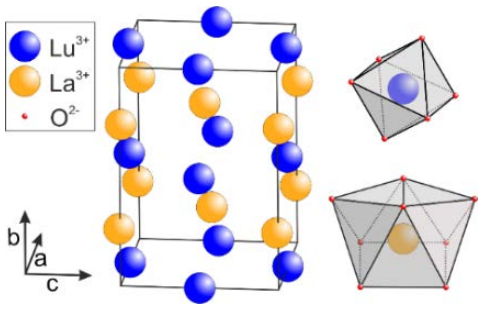

Fig. 1. Unit cell of the orthorhombic perovskite $LaLuO_3$. For better visibility oxygen atoms are omitted in the unit cell. The right side polyhedra show the LuO_6 (C_i) and LaO_8 (C_s) coordination spheres. The LuO_6 polyhedron is tilted by the actual octahedral tilt angle, while the LaO_8 polyhedron is aligned for best visibility of the symmetry.

The ionic radius of Yb^{3+} doping ions in 6-fold coordination of 0.868 Å is in excellent agreement with that of Lu^{3+}. However, in 8-fold coordination, it is about 15% smaller than La^{3+} with an ionic radius of 1.30 Å [14]. Unfortunately, the octahedral Lu^{3+}-site, on which Yb^{3+}-ions should mainly be incorporated, belongs to the inversion-symmetric C_i point group featuring low

Optical Materials EXPRESS

transition cross-sections. Nevertheless, due to the short distances of the O^{2-} anions, ranging from 2.197 Å to 2.236 Å, with an average of 2.22 Å, in this low coordinated environment [12], a strong crystal field induces a large Stark splitting of the two Yb^{3+} energy multiplets, resulting in broad spectra. On the other hand, a fraction of the Yb^{3+} ions is incorporated into the La^{3+}-site [12]. Previous reports have shown that 5-6% of lutetium atoms occupy the larger Ln (=A) site and similar anti-site occupancy is expected for Yb^{3+} due to its comparable ionic radius [2,13]. The Ln site exhibits a lower C_s symmetry and is therefore expected to promote higher transition cross-sections. However, along with the higher coordination number, the distances of the O^{2-} ions increase to values between 2.377 Å and 3.011 Å, averaging at 2.655 Å. The correspondingly reduced crystal field should yield less broadened spectra compared to Yb^{3+}-ions on Lu^{3+}-sites. It should also be noted, that the presence of such anti-sites is suggested to further reduce the symmetry to the monoclinic *Pm* space group [9]. However, the calculated monoclinic angle of 90.3° deviates only slightly from the orthorhombic value of 90° [9]. Table 1 lists parameters relevant to the spectroscopic and laser properties.

Table 1. Properties of $LaLuO_3$

Property	Value	Ref.
Structure	Orthorhombic	[11]
Space group	D_{2h}^{16} – *Pnma* (Nr. 62)[a]	[11]
Doping site	~95% Lu^{3+}, ~5% La^{3+}	[9]
Goldschmidt factor	0.800	[7,14]
Lattice parameters $LaLuO_3$	*a*: 6.0218 Å *b*: 8.3804 Å *c*: 5.8259 Å	[10]
Lattice parameters Yb(1 at.%):$LaLuO_3$	*a*: 6.0133 Å *b*: 8.3693 Å *c*: 5.8101 Å	this work
Formula units per unit cell	4	[9]
Cation symmetry	La: C_S,Lu: C_i	[1]
Coordination number	La: 8, Lu: 6	[8]
Cation ionic radius	La: 1.36 Å, Lu: 0.861 Å	[14]
Cation density	2.72×10^{22} cm^{-3} (La + Lu)	calc.
Cation mass	La: 138.9 u, Lu: 175.0 u	[15]
Band gap energy	> 5 eV	[1]
4-phonon laser limit[b]	~4.8 µm	calc.
Transparency range	< 225 nm to > 5 µm	[1,4]
Thermal conductivity	~2.5 $Wm^{-1}K^{-1}$	[16]
Density	8.18 g/cm^3 (calc. here), 8.4 g/cm^3 (exp.)	[1]
Max. phonon energy	483 cm^{-1} (calc.) 523.3 cm^{-1} (exp.)	[9,17]
Crystal field depression	19657 cm^{-1} (La-site)	[18]
Growth method	Czochralski	[2]
Melting point	2120 °C	[1]
dL/dT	*a*: 6.0×10^{-6} K^{-1} *b*: 2.7×10^{-6} K^{-1} *c*: 3.5×10^{-6} K^{-1}	[13]

[a]*Pnma* is equivalent to *Pbnm* by permuting the axes from *abc* to *cab*.
[b]assuming 4-phonon-processes to prevent lasing due to multiphonon quenching [19].

3. Crystal growth

An Yb:$LaLuO_3$ crystal was grown by the Czochralski growth method adapted for high-melting oxide crystals as described in detail *e.g.* in [2,20]. The hygroscopic starting material La_2O_3 exhibits a tendency to form carbonates and hydroxides. Therefore, the powder was dried prior

Optical Materials EXPRESS

to the preparation of the starting materials. Even though the exposure time of the La_2O_3 to ambient atmosphere was kept as short as possible, the starting material composition was weighed according to $Yb_{0.029}La_{1.03}Lu_{0.94}O_3$. This nominal excess of dried La_2O_3 powder compared to the stoichiometric composition accounted for possible carbonate and hydroxide impurities in this component, which would be unstable during heating at temperatures well below the melting point of $LaLuO_3$. Furthermore, preliminary results on undoped $LaLuO_3$ single crystals have shown that a deficiency of lanthanum oxide in the melt leads to a reduced crystalline quality.

The Yb-doped crystal was grown in an iridium crucible with an inner diameter of 38 mm and a height of 42.5 mm. To ensure suitable temperature gradients we used a 70 mm high, actively heated iridium afterheater placed above the crucible. The crucible itself was embedded in ZrO_2 granulate and the whole setup was kept in Alfrax ceramics. An iridium rod was used for seeding the crystal to initiate the growth. The crystal was grown under a flowing Ar-atmosphere with a rotation of 10 rpm and a growth rate of 0.7 mm/h for about 100 h.

The as-grown crystal is shown in Fig. 2(a). It has a length of 74 mm including the seed region and a diameter of about 18 mm at a weight of 113 g. It appears multicrystalline and cracked in the shoulder region, which we attribute to the lack of a seed crystal. In contrast, the region between ~30 mm and ~55 mm from the top is single crystalline, clear, and free of cracks. Even though only about 50% of the melt was crystallized in the boule, the bottom 20 mm of the boule is ceramic and opaque. This indicates a change of the melt composition during the growth, most likely caused by segregation, which prohibited the growth of the pure orthorhombic $LaLuO_3$ phase at a certain melt composition within the bottom part of the crystal.

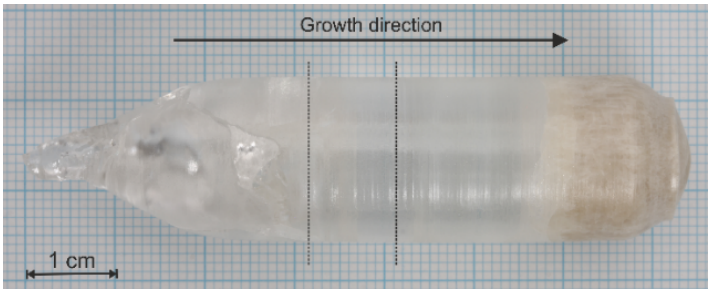

Fig. 2. Photo of the as-grown boule. Marked with dashed lines is the volume from which the laser sample was extracted.

Several samples were prepared from this boule for the different investigations performed within this work. As an example, the 6-side polished sample with dimensions of $a \times b \times c = 14 \times 10 \times 8$ mm^3 used for spectroscopy and laser experiments is shown in the inset of Fig. 4. It was extracted from the volume between the dashed vertical lines in Fig. 2.

4. Crystal characterization

4.1. Compositional characterization

First, we investigated the composition of a sample from the seed region on the left end of the crystal shown in Fig. 2 by inductively coupled plasma optical emission spectroscopy (ICP-OES) and found it to be $Yb_{0.0295}La_{0.9606}Lu_{1.0099}O_3$. As expected, despite an excess of La_2O_3 powder in the starting composition, at the very beginning of the growth our $LaLuO_3$ crystal exhibits an excess of 'small' cations (Lu + Yb = 52%) requiring ~4% anti-sites [2,12,13].

To evaluate possible segregation during the growth, a micro X-ray fluorescence (μ-XRF) mapping of the laser sample was performed with a Bruker M4 TORNADO [21] using a Rh X-ray source operated at 50 kV and 200 mA. The primary radiation was focused on the sample surface

Optical Materials EXPRESS

by a polycapillary X-ray lens to a spot size of about 20 µm. The chamber pressure was held at 20 mbar. The integration time was set to 40 ms per pixel, and 4 measurement cycles were performed.

A line scan of 13 mm (650 data points) along the a-axis on the polished a-c plane of the laser sample was extracted from this map, which is shown in the inset of Fig. 3(a). Here, the spectra of all pixels within an interval of ±0.215 µm perpendicular to the line-scan center were integrated to improve the signal-to-noise ratio.

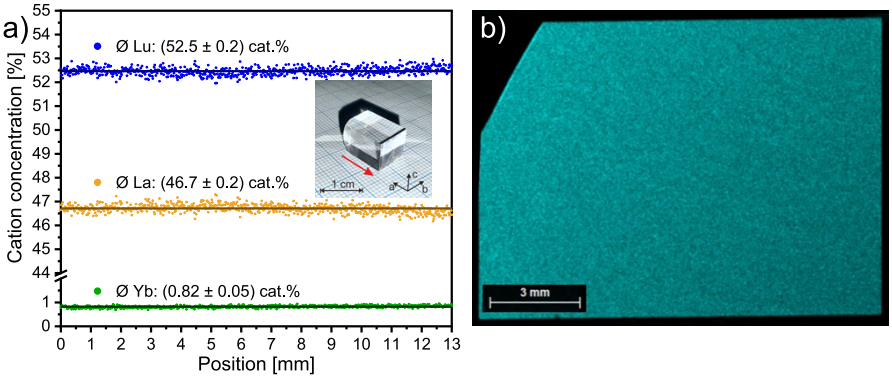

Fig. 3. (a) Results of the µ-XRF scan. The resulting average crystal composition is $Yb_{0.016}La_{0.93}Lu_{1.05}O_3$. The inset shows the laser sample, the red arrow indicates the direction of the scan. (b) EDLM mapping result of the a-c-plane indicating single-crystallinity.

The composition was quantified by the standard-free fundamental parameter approach [22]. Due to the lack of a standard reference sample for the µ-XRF investigations, the absolute values may have a systematic error, but the relative change along the growth axis is reliable. In particular, due to a partial spectral overlap of the X-ray fluorescence lines for Yb and Lu, the absolute values for Yb are subject to a large systematic uncertainty, while the sum of Yb and Lu is more reliable.

As seen in Fig. 3(a), the laser sample has an average composition of $Yb_{0.016}La_{0.93}Lu_{1.05}O_3$. We did not detect any significant segregation in this sample taken from the inner volume of the crystal. In contrast, at the surface of the as-grown crystal, we found an increased amount of La, which increased with growth progress from 51% to 53% in the range between 3 cm and 5 cm of crystal length (cf. Figure 2). This phenomenon is currently the subject of further investigations.

The cation ratio (Yb + Lu):La of 53:47 determined for the inner part of the volume is in good agreement with the ICP-OES results for the seed region of 52:48 and indicates that no strong segregation takes place during the growth. Due to the systematic error of the µ-XRF measurements and the lack of segregation, for the Yb^{3+} doping concentration we rely on the ICP-OES result and assume that our $LaLuO_3$ crystal has a homogeneous Yb^{3+}-doping concentration of 1.48 at.% with respect to both cation sites, corresponding to a doping ion density of $4.0 \times 10^{20}\,cm^{-3}$ used in the spectroscopic characterization.

Using the same µ-RFA spectrometer, we also performed energy-dispersive Laue mappings (EDLMs) as detailed in [21] to assess the microstructure. Figure 3(b) shows the results for the a-c plane for a Bragg peak at an energy of 8.1 keV. Here, different Bragg peaks indicating different crystallographic orientations would appear in different colors. The uniform Bragg peak intensity over the entire sample confirms that the laser sample is single crystalline with no high-angle grain boundaries or twins.

Optical Materials EXPRESS

The results of the compositional analyses are somewhat contrary to those of Guo et al. [5], who observed a degradation of the crystal quality already for La cation contents exceeding 45.2% and only polycrystalline growth for more than 48.1% of La in OFZ-grown $LaLuO_3$.

4.2. Structural characterization

The structure of the Yb^{3+}:$LaLuO_3$ crystal was characterized by single-crystal and powder X-ray diffraction (XRD) to determine lattice parameters, atomic positions, and, in particular, occupancies of Ln (A-site, La) and Ln' (B-site, Lu) sites. While powder XRD is generally preferred for determining lattice parameters, single-crystal XRD offers higher reliability for analyzing the site occupancies.

4.2.1. Powder X-ray diffraction

To enhance the elemental sensitivity between La and Lu and thus assist the determination of the site occupancies, the powder XRD measurements were performed using two different STOE STADI MP diffractometers at different wavelengths.

The first, equipped with a Cu X-ray source fitted with a curved Ge (111) monochromator ($\lambda = 1.5406$ Å) and a DECTRIS MYTHEN2 R detector, was used in a modified Debye-Scherrer geometry. Diffraction patterns were measured in the range of 0–99° 2Θ ($Q = 0$–6.2 Å^{-1}) for a duration of 0.5 h per data point.

The second diffractometer was equipped with a Mo X-ray source fitted with a curved Ge (111) monochromator ($\lambda = 0.70926$ Å) and a DECTRIS MYTHEN R detector in a flat-plate transmission geometry. Diffraction patterns were measured in the range of 0–54° 2Θ ($Q = 0$–8.04 Å^{-1}) for a duration of 0.3 h per data point.

Samples for both measurements were prepared by grinding a small piece of the single crystal boule (taken from an area close to the left vertical black line in Fig. 2) in a mortar. The resulting powder was loaded in a 0.5 mm capillary for the Cu-XRD and spread into a thin coating for the Mo-XRD measurement.

Both powder XRD diffraction patterns shown in Fig. 4 were analyzed by a simultaneous Rietveld refinement using the GSAS-II software package [23]. The starting CIF file of $LaLuO_3$ with *Pnma* space group was taken from [24]. The background was approximated using Chebyshev polynomials, and the instrument function was calibrated by empirically fitting the Caglioti functions with included asymmetry to a NIST Si standard measured in the same geometry on both diffractometers. The sample absorption was estimated according to Cromer and Liberman [25]. In the refinements, unit cell parameters, microstrain, atomic positions, occupancies, and thermal displacements were optimized. During the occupancy optimization, the bulk composition was constrained to match the results of the ICP measurement. Moreover, Yb ($Z = 70$) was assumed to have identical scattering properties to Lu ($Z = 71$).

The *Pnma* orthorhombic cell was optimized to lattice parameters of $a = 6.01333(2)$ Å, $b = 8.36939(3)$ Å, $c = 5.81006(2)$ Å, and a calculated density of $\rho = 8.208$ g/cm^3. No evidence of potential distortion towards the *Pm* monoclinic system was observed within the accuracy of the two measurements. Most notably, the fraction of Lu ions on La sites was calculated as 7.9%, while 3.9% of the La ions were found on Lu sites. This is in very good agreement with the compositional analyses presented in the previous section. Due to similarities between Yb and Lu, we assume, that Yb exhibits a very similar distribution ratio between the two sites. Some small inaccuracies could have been induced by the very high absorbance of the sample in the Cu-XRD measurements, yielding imperfect data quality. Therefore, we consider the single-crystal XRD presented in the following section to provide more reliable results in this aspect.

Optical Materials EXPRESS

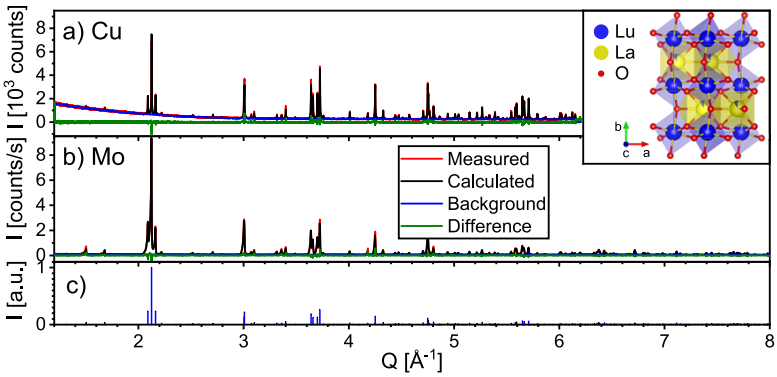

Fig. 4. Refinements of the powder XRD patterns of Yb^{3+}:$LaLuO_3$ obtained with Cu- (a) and Mo- (b) instruments along with the predicted intensities (c). The inset shows the calculated structure.

4.2.2. Single-crystal X-ray diffraction

In addition, single-crystal diffraction experiments were conducted to validate the powder XRD results. For the measurements, a clear and colorless piece of Yb^{3+}:$LaLuO_3$ with dimensions of $34 \times 43 \times 48$ µm^3 was extracted from the boule by breaking a part of it using an agate mortar. No cracks, inhomogeneities, or twinning could be observed under polarized light. The sample was then mounted onto a Microloop sample holder (Jena Bioscience, Ø = 100 µm) on a goniometer head.

The data were collected on a Bruker D8 VENTURE system equipped with a Photon II 7 detector, a multilayer monochromator and a Mo Kα Incoatec microfocus sealed tube source ($\lambda = 0.71073$ Å). The measurements were conducted as combined φ and ω scans at 180 K. A total of 1543 frames were collected with a total exposure time of 18.38 hours. The frames were integrated using the Bruker SAINT software package and a wide-frame algorithm. An orthorhombic unit cell was used and the integration yielded 48,881 reflections to a maximum θ angle of 79.51° yielding 0.36 Å resolution. The unit cell constants are based on the refinement of the xyz-centroids of 9924 reflections above $20\sigma(I)$ with $8.536° < 2\theta < 154.6°$. The measured data were corrected for absorption effects using the multi-scan method (SADABS). The ratio of minimum to maximum apparent transmission was 0.607. The space group was determined using XPREP [26] and by systematic extinctions, the space group *Pnma* was confirmed. For further structure solution and refinement, the SHELX software suite [26] was used. The thermal displacement parameters were refined isotropically and towards the end of the refinement, a weighting scheme was applied.

To determine the concentration of anti-site cations on the respective sites, a mixed occupancy of both, La and Lu sites, was allowed. The results corroborate those of the powder diffraction measurements. The lattice constants were determined as $a = 6.0167(3)$ Å, $b = 8.3686(4)$ Å, $c = 5.8138(3)$ Å with a unit cell volume of 292.73(3) Å^3. The concentration of Lu anti-sites on the La-site is calculated as 4-5 at.%.

Both XRD methods thus provide very consistent results within the range of error and determine that Yb^{3+}:$LaLuO_3$ belongs to the *Pnma* space group. Neither method finds any evidence of a potential distortion towards *Pm* symmetry, including at 180 K, contradicting previous suggestions [9]. Both methods also find a very similar degree of anti-sites with Lu – and thus Yb – on La sites (A-site of C_S symmetry) as 7.9 at.% and 4-5 at.% for powder and single-crystal XRD respectively, where the latter is considered to be more reliable for the reasons mentioned above and in good agreement with previous literature [2,13].

Optical Materials EXPRESS

4.3. Spectroscopic characterization

4.3.1. Absorption cross sections

For the determination of the absorption cross-sections we performed polarized transmission measurements using a UV-VIS spectrophotometer (Perkin Elmer, Lambda 1050) using the $14 \times 10 \times 8$ mm^3 sample shown in Fig. 2(d). All six facets of the sample were polished to laser quality, giving access to all polarizations, *i.e.*, all orientations of the electric and magnetic field vectors with respect to the crystal axes. The transmission in the range not affected by Yb^{3+} absorption, *e.g.*, around 1150 nm, amounted to ~80% in all cases. This permits a rough estimation of the refractive index as 1.95 ± 0.04 for all polarizations by assuming Fresnel reflection losses on both sample surfaces. This value is higher than the values found *e.g.* for the cubic sesquioxide Lu_2O_3 [27], but realistic given the value of 2.0 found for the isostructural $DyScO_3$ [28].

We measured the transmission for horizontal and vertical light polarization for all three facets. The resulting six spectra are shown in Fig. 5(a-c). Assuming the usual case of electric dipole transitions to dominate the absorption, one should obtain three sets of two identical spectra each. However, the absorption spectra for the electric field vector **E** oriented parallel to the same axis on different facets differ considerably. The only difference *e.g.* between the spectra for **E**||a-polarization measured along the 001- (c-axis) and 010-directions (b-axis) is the orientation of the magnetic field vector **H**, which is **H**||b and **H**||c, respectively. Thus, the differences in the spectra must originate from magnetic dipole transitions. The contribution of these magnetic dipole transitions is remarkable in Yb^{3+}:$LaLuO_3$. The data do not allow to determine absolute values [29], but subtracting *e.g.* the two spectra shown in Fig. 5(c) for **E**||c yields the difference between the magnetic dipole contribution for **H**||a and **H**||b. This difference, shown in green below each absorption curve, reaches 80% of the value for the blue curve (**E**||c, **H**||b) suggesting that the strength of the magnetic dipole transitions is of the same order of magnitude or even higher than the electric dipole transitions in Yb^{3+}:$LaLuO_3$. This is explained by the majority of the Yb^{3+} being incorporated on the inversion symmetric Lu^{3+}-sites with C_i point group, for which electric dipole transitions are forbidden. Figure 5(d) shows the sums of all red and all blue curves in Fig. 5(a-c), thus the sums of all three polarizations of **E** and **H**. Both curves are identical, which indicates our crystal is properly oriented and the polarization of the light was well adjusted to the crystallographic axes.

Assuming an Yb^{3+}-ion density of 4.0×10^{20} cm^{-3} the absorption cross sections were calculated from the absorption coefficients. The resulting values are shown on the right y-axis in Fig. 5(a-c). The highest absorption cross section peak of 4.2×10^{-21} cm^2 is found in **E**||b-orientation and mostly independent on the **H**-polarization at a peak wavelength of 983.2 nm. For the other two orientations **E**||a and **E**||c, the highest absorption cross-sections are significantly lower and amount to 2.5 and 2.0×10^{-21} cm^2, respectively, found at 971 nm in both cases, but strongly depending on the orientation of the **H**-vector. It is worth noting that these absorption cross sections are comparably high given the inversion symmetry of the main site for the Yb^{3+} ions and the long fluorescence lifetimes discussed in the next chapter. In fact, the peak absorption cross sections for Yb^{3+}:YAG amount to 8×10^{-21} cm^2 [30], which is less than twice that of Yb^{3+}:$LaLuO_3$.

4.3.2. Emission properties

To evaluate the emission properties, the fluorescence spectra of the Yb^{3+}:$LaLuO_3$ sample were recorded in four of the six different possible orientations of the electric and magnetic field vectors to the axes. The sample was excited at a wavelength of 862.5 nm by a wavelength-tunable Ti:sapphire laser (SolsTiS, MSquared Lasers) and the fluorescence was recorded using a grating monochromator (M1000, HORIBA) and a near-infrared sensitive photomultiplier tube (R5108, Hamamatsu). After correction for the polarization-dependent response of the setup, the data were evaluated using a combination of the McCumber relation [31] and the Füchtbauer-Ladenburg

Optical Materials EXPRESS

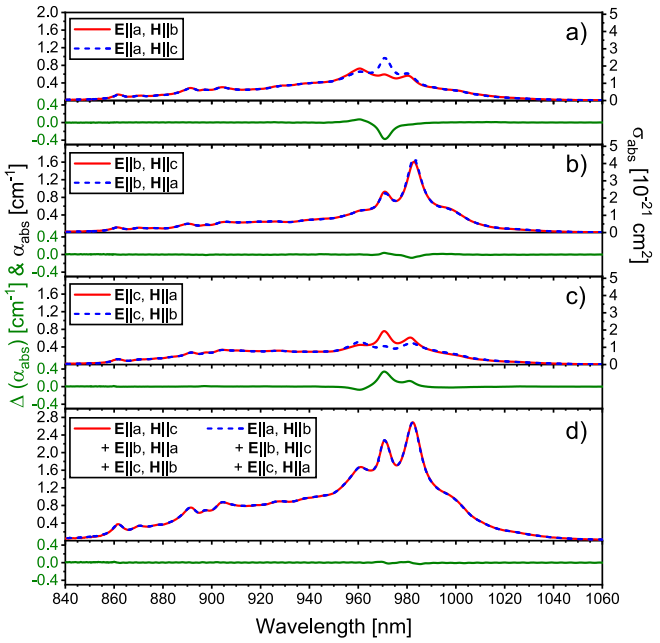

Fig. 5. (a-c) Absorption coefficients (left axis) and absorption cross sections (right axis) for all 6 orientations of the electric field vector **E** and magnetic field vector **H** with respect to the crystal axes of Yb^{3+}:$LaLuO_3$. The green lines below each graph shows the difference between the red and the blue curve attributed to magnetic dipole components. (d) The sums of all red and all blue curves in (a-c) match, indicating a correct orientation of the sample.

(FL) equation [32–34]. The results are shown in Fig. 6(a-c). In the shorter wavelength range below 1010 nm, where the fluorescence signal is strongly affected by reabsorption, we utilized the outcome of the McCumber relation. In contrast, in the long wavelength range, the signal-to-noise ratio of the McCumber relation results suffers from a low absorption signal. Therefore, in this range the fluorescence signal was multiplied by a factor of λ^5 according to the proportionality between spontaneous fluorescence and stimulated emission in the FL equation and normalized it to the value obtained by the McCumber relation at 1010 nm.

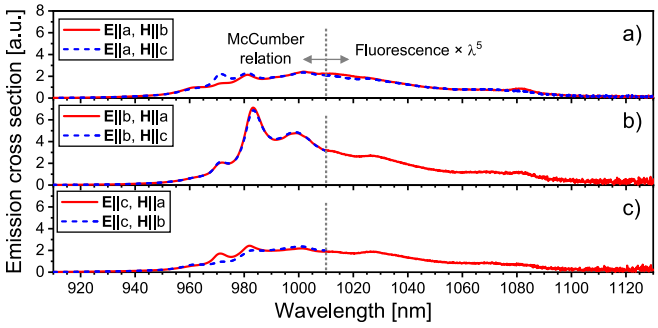

Fig. 6. (a-c) Polarized stimulated emission cross section spectra of Yb^{3+}:$LaLuO_3$ in arbitrary units. As indicated by the dotted horizontal line, values below 1010 nm were determined from the absorption spectra by the McCumber relation [31], those for longer wavelengths by multiplying the measured fluorescence spectra by λ^5 following the Füchtbauer-Ladenburg equation [32–34].

Optical Materials EXPRESS

As expected, depending on the orientation of the magnetic field vector **H**, we obtained two different fluorescence spectra for **E**||a polarization. However, due to the small differences in the absorption spectra in both orientations of the **H**-vector for **E**||b and **E**||c the range of possible laser wavelengths above 1000 nm, we did not record the fluorescence in all possible orientations of **H** as only minor deviations are expected.

We were not able to determine precise absolute values for the stimulated emission cross sections due to the Yb^{3+} ions occupying two sites in $LaLuO_3$. The McCumber relation requires a single set of Stark level positions and the FL method requires one single value for the fluorescence lifetime. Both cannot be precisely stated for multi-site host materials.

Nevertheless, the shape of the spectra resembles the stimulated emission cross section spectra and the relative intensity among polarizations is accurate. By using the 'average' integrated lifetime of 1.46 ms determined in the next section as an input parameter for the FL method, a reasonable estimation of the cross section magnitude can be made by scaling the spectra with a factor of 10^{-21} cm^2. The McCumber relation resembles these values assuming a realistic partition function ratio of 0.89.

All spectra are smooth and extend to wavelengths well beyond 1090 nm with prominent features at around 1030 nm and 1080 nm in the range of expected lasing wavelengths. The highest cross-sections are found for **E**||b polarization, where according to the results of the absorption measurements no strong dependence on the orientation of the **H**-vector is expected.

4.3.3. Gain cross sections

Even without absolute values for the emission cross-sections, the data shown in Fig. 5(a-c) and Fig. 6(a-c) enable the calculation of gain spectra by using the equation:

$$\sigma_{gain} = \beta \cdot \sigma_{em} - (1 - \beta) \cdot \sigma_{abs} \tag{1}$$

where β is the inversion level, *i.e.*, the fraction of ions in the excited state. It should, however, be noted that without absolute values for the emission cross-sections, the inversion levels required for a certain gain shape are only meaningful as relative quantities.

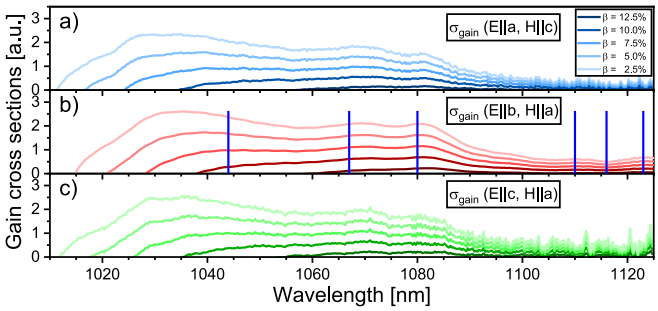

Fig. 7. (a-c) Polarization-dependent gain cross sections of Yb^{3+}:$LaLuO_3$ for different inversion levels β. The spectra for **E**||b were smoothened to improve visibility. The vertical blue lines mark the observed laser wavelengths.

The resulting gain spectra indicate a broad potential range of laser wavelengths, ranging from ~1010 nm to at least 1090 nm. For low inversion levels, *i.e.*, low output coupler transmission, gain is first achieved around 1080 nm. As the inversion level increases, the peak of the gain spectrum shifts toward ~1030 nm. In all polarizations, the gain spectra are smooth with a full width at half maximum (FWHM) exceeding 60 nm. The highest gain is found for **E**||b-polarization, suggesting that lasing is most likely to occur in this orientation.

Optical Materials EXPRESS

4.3.4. Fluorescence lifetimes

To minimize the influence of reabsorption on the fluorescence lifetime measurements, we applied the pinhole method [35,36]. The same detection setup was used, while the sample was excited by a 5-ns, 10-Hz optical parametric oscillator (OPO, GWU versaScan) tuned to an excitation wavelength of 970 nm. The fluorescence decay curves were recorded at a wavelength of 1002 nm using a Si-detector attached to a grating spectrometer. To increase the signal intensity, we used a 100 kΩ series resistance yielding a time constant of 30 µs. The pump signal was separated from the signal by a dichroic mirror.

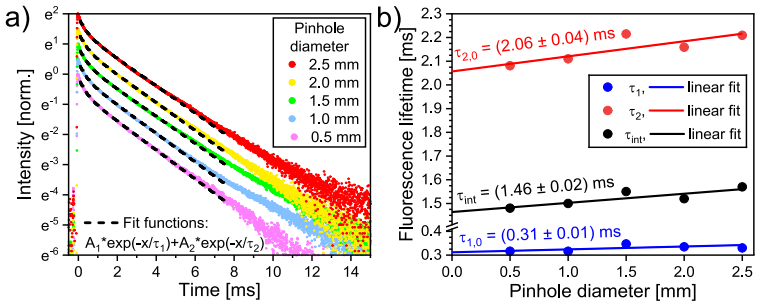

Fig. 8. (a) Logarithmic fluorescence decay curves of Yb:$LaLuO_3$ under 970-nm OPO excitation for different pinhole diameters and bi-exponential fits. For better visibility, after normalization an offset was added to the decay signal. (b) Linear extrapolation to zero pinhole diameter of the fit-results obtained from the fits shown in part (a) of this figure.

The resulting decay curves are shown in Fig. 8(a) for different pinhole diameters between 0.5 mm and 2.5 mm. The decay curves are clearly non-single-exponential, but a bi-exponential fit provided a good approximation to the data. To eliminate any influence from the resistor, the fits shown in Fig. 8(a) start 0.1 ms after the maximum signal intensity. The fit range was limited to 7.5 ms due to electronic background artifacts seen e.g. for the curve recorded with a pinhole diameter of 1.5 mm.

The bi-exponential fits yield a fast decay constant τ_1 below 0.35 ms with reproducible amplitudes of ~0.38 and a slow decay constant τ_2 of more than 2 ms with larger amplitudes of ~0.62 for all pinhole diameters. In all bi-exponential fits, the error was below 1% for all parameters. We also calculated the integrated lifetimes $\tau_{int} = \int I(t)dt/I(0)$ in the range between 0.1 and 7.5 ms. The linear extrapolations of the fluorescence lifetimes to zero pinhole diameter τ_0 for all three cases are shown in Fig. 8(b) and yield lifetimes of 0.31 ms and 2.06 ms for the fast and slow component, respectively. As expected, the 'average' integrated lifetime of 1.46 ms is between these values.

A similar bi-exponential decay was previously observed for low-doped sesquioxide crystals, where also two different sites are available for the Yb^{3+} ion [37]. It is thus reasonable to assign the two different lifetimes to the two sites of the perovskite structure, where the longer lifetime originates from Yb^{3+}-ions occupying the smaller, inversion symmetric C_i-site and the shorter lifetime is that of Yb^{3+}-ions on C_S-sites. While 0.31 ms is a short lifetime for an Yb^{3+}-doped material, such values have been previously reported in other systems, *e.g.*, for Yb:KYW [38]. Also other perovskite crystals with Yb^{3+}-ions mainly on C_S sites such as Yb:YAP exhibit short lifetimes below 0.6 ms [39]. These findings support the conclusion that the low symmetry of this site strongly releases the Laporte rule for the 4*f* transitions. On the other hand, 4*f* transitions of Yb^{3+} ions on the highly symmetric C_i-site remain strongly parity forbidden. Consequently, a very long lifetime of more than 2 ms, similar to that of Yb^{3+} in fluoride crystals [40] or oxyborates [41] is consistent with expectations.

Optical Materials EXPRESS

5. Laser experiments

For the laser experiments we utilized a linear nearly plane-concave cavity as seen in Fig. 9. We used a plane pump mirror M1, which was highly transparent for the pump wavelength, but highly reflective in the range of potential laser wavelengths. The output coupling mirrors M2 had radii of curvature of 50 mm and transmissions between 0.4% and 6.5% for the respective laser wavelength. The detailed transmission characteristics of the output couplers are found in Fig. 10(b).

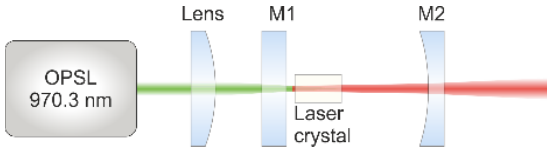

Fig. 9. Schematic of the laser setup. M1: Input coupling mirror, M2: Output coupling mirror.

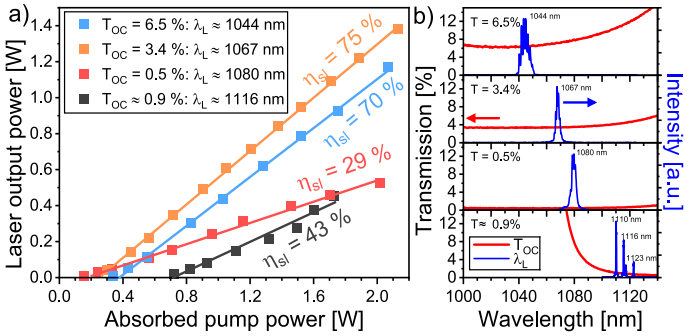

Fig. 10. (a) Laser characteristics of Yb^{3+}(1.48 at.%):$LaLuO_3$ for different output coupler transmissions T_{OC}. (b) Laser spectra (blue) and wavelength dependent transmission (red) for the different output coupling mirrors.

The gain medium was a c-cut (optical axis parallel to (001)) Yb^{3+}(1.48 at.%):$LaLuO_3$ crystal with a length of 8 mm, and an aperture of 10×14 mm^2 as seen in Fig. 3. Accounting for the refractive index of the laser sample, the optimum cavity length was found to be 55 mm.

As the pump source, we employed a tunable optically pumped semiconductor laser (OPSL, Coherent) [42] delivering a maximum output power of ~5 W with a good beam quality ($M^2 < 3$) tuned to a wavelength of 970.3 nm. At this pump wavelength, the laser sample absorbed about 50% of the pump light in single pass. The highest absorption peak at 983 nm was not within the tuning range of our pump source, moreover the transmission of our pump mirror would start to decrease at such long pump wavelengths. The pump light was focused into the crystal with a lens with a focal length of 75 mm yielding a pump spot diameter of about $40 \times 60\,\mu$m^2 in the laser crystal. This cavity configuration and pump radius strongly favored fundamental mode operation. Indeed, we observed the characteristic TEM_{00} mode transforming into clean TEM_{01} or higher modes under intentional misalignment.

Figure 10(a) shows the laser characteristics. The highest slope efficiency of 75% was obtained with an output coupling mirror with a transmission of $T_{OC} = 3.4\%$, yielding a laser wavelength of 1067 nm. In this case, the output power amounted to 1.38 W under 2.13 W of absorbed pump power, corresponding to an optical-to-optical efficiency of 65%. For this mirror, the laser threshold pump power was reached at 0.41 W. The upper limit for the slope efficiency η_{sl} is given

Optical Materials EXPRESS

by the product of the Stokes efficiency, *i.e.,* the ratio of pump and laser wavelength, $\eta_{St} = \lambda_p/\lambda_{las}$ and the resonator efficiency $\eta_{res} = T/(T + L)$. These equations allow to estimate an upper limit for the resonator losses of $L < 0.7\%$, proving the high quality of our Yb:$LaLuO_3$ crystal.

As seen in Fig. 10(a), other output coupling mirrors yielded lower slope efficiencies. However, Fig. 10(b) shows the laser wavelength in comparison to the output coupling mirror (M2) transmission characteristics. It can be seen that even with relatively flat transmission characteristics the laser operated in a wide range of wavelengths between 1044 nm and 1080 nm indicating a broad and smooth gain profile. Utilizing an output coupler with a higher transmission for wavelengths below 1080 nm, we even obtained lasing at wavelengths up to 1123 nm, which is a remarkably long laser wavelength for an Yb^{3+}-doped gain crystal. In this case, we obtained simultaneous lasing on three distinguished lines at 1110 nm, 1116 nm and 1123 nm as seen in Fig. 10(c). Due to the lower gain at such long wavelengths, the laser threshold increased from below 0.2 W for the lowest output coupler transmission of 0.5% to 0.72 W at the longest wavelengths. Nevertheless, the slope efficiency remained as high as 43%. In all cases, the laser output was polarized parallel to the b-axis of the crystal, which is in agreement with the gain spectra shown in Fig. 7. The full laser emission bandwidth exceeded 5 nm at 1044 nm, 1067 nm and 1080 nm, which points towards inhomogeneous broadening mechanisms.

6. Conclusion

We grew a large boule of Yb:$LaLuO_3$ with high optical quality. X-ray diffraction confirmed its *Pnma* structure and chemical analyses revealed no segregation in the investigated volume of the crystal. According to our XRD data, approximately 3% of Lu ions occupy La sites in the grown crystal.

Spectroscopic investigations further confirm the presence of about 4-5% of Yb^{3+} ions on anti-sites, as evidenced by a bi-exponential fluorescence decay. The slow component with a lifetime of 2.06 ms corresponds to Yb^{3+} ions on inversion-symmetric Lu-sites with $C_i$symmetry, while the fast component of 0.31 ms is associated with anti-site Yb^{3+} ions on La-sites with C_s symmetry. Absorption measurements reveal a strong magnetic dipole contribution, attributed to the majority of Yb^{3+} ions being incorporated on inversion-symmetric C_s sites for which electric dipole transitions are parity-forbidden.

Despite this, the absorption and emission cross sections are only by about a factor of two lower than those of the widely used laser gain material Yb^{3+}:YAG. In contrast to Yb^{3+}:YAG, Yb^{3+}:$LaLuO_3$ exhibits exceptionally smooth and broad emission bands exceeding 60 nm in width. In the first laser experiments utilizing the new laser crystal, we achieved high slope efficiencies of up to 75% across a broad wavelength range from 1044 nm to 1123 nm.

These findings highlight the potential of Yb:$LaLuO_3$ as a promising gain material for femtosecond pulse generation in mode-locked oscillators and for widely tunable lasers in the 1.1 µm wavelength range.

Acknowledgments. The authors acknowledge support of Albert Kwasniewski (IKZ) in orientating the crystal and Michael Schulze (IKZ) for useful hints on compositional adjustments for the growth process. Moreover, we thank Valentin Petrov at Max-Born-Institute in Berlin for helpful discussions concerning the spectroscopy.

Disclosures. The authors declare no conflicts of interest.

Data availability. Data underlying the results presented in this paper are not publicly available at this time but may be obtained from the authors upon request.

References

1. K. L. Ovanesyan, A. G. Petrosyan, G. O. Shirinyan, *et al.*, "Single crystal growth and characterization of $LaLuO_3$," Opt. Mater. (Amsterdam, Neth.) **10**(4), 291–295 (1998).
2. R. Uecker, R. Bertram, M. Brützam, *et al.*, "Large-lattice-parameter perovskite single-crystal substrates," J. Cryst. Growth **457**, 137–142 (2017).
3. J. Varghese, T. Joseph, M. T. Sebastian, *et al.*, "Crystal Structure and Microwave Dielectric Properties of $LaLuO_3$ Ceramics," J. Am. Ceram. Soc. **93**(10), 2960–2963 (2010).

Optical Materials EXPRESS

4. L. Zhang, C. Madej, C. Pedrini, *et al.*, "Elaboration and spectroscopic properties of new dense cerium-doped lutetium based scintillator materials," Chem. Phys. Lett. **268**(5-6), 408–412 (1997).
5. R. Q. Guo, F. Y. Wang, S. X. Wang, *et al.*, "Exploration of the Crystal Growth and Crystal-Field Effect of Yb^{3+} in Orthorhombic $GdScO_3$ and $LaLuO_3$ Crystals," Cryst. Growth Des. **23**(5), 3761–3768 (2023).
6. C. Kränkel, A. Uvarova, C. Guguschev, *et al.*, "Rare-earth doped mixed sesquioxides for ultrafast lasers," Opt. Mater. Express **12**(3), 1074–1091 (2022).
7. V. M. Goldschmidt, "Die Gesetze der Krystallochemie," Naturwissenschaften (1913-2014) **14**(21), 477–485 (1926).
8. M. Bharathy, A. H. Fox, S. J. Mugavero, *et al.*, "Crystal growth of inter-lanthanide $LaLn'O_3$ (Ln' = Y, Ho–Lu) perovskites from hydroxide fluxes," Solid State Sci. **11**(3), 651–654 (2009).
9. S. Coh, T. Heeg, J. H. Haeni, *et al.*, "Si-compatible candidates for high-κ dielectrics with the *Pbnm* perovskite structure," Phys. Rev. B **82**(6), 064101 (2010).
10. K. Ito, K. Tezuka, and Y. Hinatsu, "Preparation, magnetic susceptibility, and specific heat on interlanthanide perovskites ABO_3 (A = La-Nd, B = Dy-Lu)," J. Solid State Chem. **157**(1), 173–179 (2001).
11. H. Müller-Buschbaum and P. H. Graebner, "Crystal structure of $LaErO_3$ and $LaLuO_3$," Z. Anorg. Allg. Chem. **386**(2), 158–162 (1971).
12. D. G. Schlom, L. Q. Chen, X. Q. Pan, *et al.*, "A thin film approach to engineering functionality into oxides," J. Am. Ceram. Soc. **91**(8), 2429–2454 (2008).
13. K. L. Ovanesyan, A. G. Petrosyan, G. O. Shirinyan, *et al.*, "Czochralski single crystal growth of Ce- and Pr-doped $LaLuO_3$ double oxide," J. Cryst. Growth **198-199**, 497–500 (1999).
14. R. D. Shannon, "Revised effective ionic radii and systematic studies of interatomic distances in halides and chalcogenides," Acta Crystallogr., Sect. A **32**(5), 751–767 (1976).
15. T. Prohaska, J. Irrgeher, J. Benefield, *et al.*, "Standard atomic weights of the elements 2021," Pure Appl. Chem. **94**(5), 573–600 (2022).
16. E. Langenberg, E. Ferreiro-Vila, V. Leborán, *et al.*, "Analysis of the temperature dependence of the thermal conductivity of insulating single crystal oxides," APL Mater. **4**(10), 104815 (2016).
17. Y. Y. Wang, Z. M. Qi, T. Shao, *et al.*, "Infrared phonon modes and local structure of amorphous and crystalline $LaLuO_3$ thin films," J. Alloys Compd. **571**, 103–106 (2013).
18. P. Dorenbos, "The 5d level positions of the trivalent lanthanides in inorganic compounds," J. Lumin. **91**(3-4), 155–176 (2000).
19. H. W. Moos, "Spectroscopic relaxation processes of rare earth ions in crystals," J. Lumin. **1-2**, 106–121 (1970).
20. R. Uecker, B. Velickov, D. Klimm, *et al.*, "Properties of rare-earth scandate single crystals (RE = Nd - Dy)," J. Cryst. Growth **310**(10), 2649–2658 (2008).
21. C. Guguschev, R. Tagle, U. Juda, *et al.*, "Microstructural investigations of $SrTiO_3$ single crystals and polysilicon using a powerful new X-ray diffraction surface mapping technique," J. Appl. Crystallogr. **48**(6), 1883–1888 (2015).
22. J. Sherman, "The theoretical derivation of fluorescent X-ray intensities from mixtures," Spectrochim. Acta **7**(1), 283–306 (1955).
23. B. H. Toby and R. B. Von Dreele, "*GSAS-II*: the genesis of a modern open-source all purpose crystallography software package," J. Appl. Cryst. **46**(2), 544–549 (2013).
24. K. Nomura, T. Takeuchi, H. Kageyama, *et al.*, "High temperature crystallographic study of $(La_{0.9}Sr_{0.1}M^{III}O_{3-\delta}$ (M^{III}=Sc, In, and Lu)," Solid State Ionics **162-163**, 99–104 (2003).
25. D. T. Cromer and D. A. Liberman, "Anomalous dispersion calculations near to and on the long-wavelength side of an absorption-edge," Acta Crystallogr., Sect. A **37**(2), 267–268 (1981).
26. G. M. Sheldrick, "A short history of *SHELX*," Acta Crystallogr., Sect. A:Found. Crystallogr. **64**(1), 112–122 (2008).
27. D. E. Zelmon, J. M. Northridge, N. D. Haynes, *et al.*, "Temperature-dependent Sellmeier equations for rare-earth sesquioxides," Appl. Opt. **52**(16), 3824–3828 (2013).
28. E. Chernova, O. Pacherova, T. Kocourek, *et al.*, "Optical properties of ferroelectric epitaxial $K_{0.5}Na_{0.5}NbO_3$ films in visible to ultraviolet range," PLoS One **11**(4), e0153261 (2016).
29. T. Taminiau, S. Karaveli, N. F. van Hulst, *et al.*, "Quantifiying the magnetic nature of light emission," Nat. Commun. **3**(1), 979 (2012).
30. K. Beil, S. T. Fredrich-Thornton, F. Tellkamp, *et al.*, "Thermal and laser properties of Yb:LuAG for kW thin disk lasers," Opt. Express **18**(20), 20712–20722 (2010).
31. D. E. McCumber, "Einstein relations connecting broadband emission and absorption spectra," Phys. Rev. **136**(4A), A954–A957 (1964).
32. C. Füchtbauer, G. Joos, and O. Dinkelacker, "Über Intensität, Verbreiterung und Druckverschiebung vor Spektrallinien, insbesondere der Absorptionslinie 2537 des Quecksilbers," Ann. Phys. **376**(9-12), 204–227 (1923).
33. R. Ladenburg, "Die quantentheoretische Deutung der Zahl der Dispersionselektronen," Z. Physik **4**(4), 451–468 (1921).
34. G. Huber, W. W. Kruhler, W. Bludau, *et al.*, "Anisotropy in laser performance of NdP_5O_{14}," J. Appl. Phys. **46**(8), 3580–3584 (1975).
35. C. Kränkel, D. Fagundes-Peters, S. T. Fredrich, *et al.*, "Continuous wave laser operation of Yb^{3+}:YVO_4," Appl. Phys. B **79**(5), 543–546 (2004).
36. H. Kühn, S. T. Fredrich-Thornton, C. Kränkel, *et al.*, "Model for the calculation of radiation trapping and description of the pinhole method," Opt. Lett. **32**(13), 1908–1910 (2007).

Optical Materials EXPRESS

37. S. Kalusniak, A. Uvarova, I. Arlt, *et al.*, "Growth, characterization, and efficient laser operation of Czochralski- and micro-pulling-down-grown Yb^{3+}:$YScO_3$ mixed sesquioxides," Opt. Mater. Express **14**(2), 304–318 (2024).
38. G. Métrat, M. Boudeulle, N. Muhlstein, *et al.*, "Nucleation, morphology and spectroscopic properties of Yb^{3+}-doped $KY(WO_4)_2$ crystals grown by the top nucleated floating crystal method," J. Cryst. Growth **197**(4), 883–888 (1999).
39. G. Boulon, Y. Guyot, H. Canibano, *et al.*, "Characterization and comparison of Yb^{3+}-doped $YAlO_3$ perovskite crystals (Yb:YAP) with Yb^{3+}-doped $Y_3Al_5O_{12}$ garnet crystals (Yb:YAG) for laser application," J. Opt. Soc. Am. B **25**(5), 884–896 (2008).
40. S. Püschel, S. Kalusniak, C. Kränkel, *et al.*, "Temperature-dependent radiative lifetime of Yb:YLF: refined cross sections and potential for laser cooling," Opt. Express **29**(7), 11106–11120 (2021).
41. C. Kränkel, R. Peters, K. Petermann, *et al.*, "Efficient continuous-wave thin disk laser operation of Yb:$Ca_4YO(BO_3)_3$ in EIIZ and EIIX orientations with 26 W output power," J. Opt. Soc. Am. B **26**(7), 1310–1314 (2009).
42. M. Kuznetsov, F. Hakimi, R. Sprague, *et al.*, "High-power (>0.5-W CW) diode-pumped vertical-external-cavity surface-emitting semiconductor lasers with circular TEM00 beams," IEEE Photon. Technol. Lett. **9**(8), 1063–1065 (1997).